

Unconventional room-temperature carriers in the triangular-lattice Mott insulator TbInO_3

Received: 29 August 2022

Accepted: 13 July 2023

Published online: 17 August 2023

 Check for updates


Taek Sun Jung ^{1,8}, Xianghan Xu ^{2,3,7,8}, Jaewook Kim ^{2,3,4,8}, Beom Hyun Kim ⁵,
Hyun Jun Shin ¹, Young Jai Choi ¹, Eun-Gook Moon ⁶ ,
Sang-Wook Cheong ^{2,3}  & Jae Hoon Kim ¹ 

The strong correlations between electrons in Mott insulator materials may produce highly entangled many-body states with unconventional emergent excitations. The signatures of such excitations, if any, are commonly believed to be observable only at low temperatures. Here, we challenge this common belief and show using terahertz time-domain spectroscopy that exotic carriers exist even at room temperature in TbInO_3 , a candidate material for realizing a low-temperature quantum spin-liquid phase. In particular, over the entire temperature range of 1.5–300 K, we observe a quadratic frequency dependence in the real part of the in-plane optical conductivity as well as Fano asymmetry of an optical phonon mode strongly interacting with the excitation continuum. These features are robust even under external magnetic fields of up to 7 T. Our data confirm the presence of emergent charge carriers within the Mott charge gap of TbInO_3 , suggesting that it is possible to probe and manipulate highly entangled quantum many-body states at room temperature.

Massively entangled many-body states can be hosted by Mott insulators^{1–5}. Well-known examples include quantum spin liquids (QSLs) originating from strong frustration and correlation effects. Once doped, these may become non-Fermi liquids^{6–11}. The massive entanglement in Mott insulators may be characterized by exotic emergent excitations, such as spinons and gauge fields of QSLs, whose signatures have been reported in candidate systems of two-dimensional triangular, kagome and honeycomb lattices as well as in three-dimensional pyrochlore and hyperkagome structures^{12–16}. For example, studies of inelastic neutron scattering have identified excitation continua in candidate materials such as $\alpha\text{-RuCl}_3$ and herbertsmithite ($\text{ZnCu}_3(\text{OH})_6\text{Cl}_2$), although their interpretation is far from being complete due to disorder and impurity issues^{17,18}. Likewise, Raman studies on $\alpha\text{-RuCl}_3$ hint at QSL behaviour,

as indicated by the Fano interaction between the magnetic excitation continuum and optical phonons^{19–22}.

The dynamics of exotic emergent excitations in Mott insulators is qualitatively different from that of electrons in band insulators. Whereas electrons couple to an external electromagnetic field via the minimal coupling with the electromagnetic potentials, exotic emergent excitations are charge-neutral, which prohibits the minimal coupling (Fig. 1a). In this context, terahertz optical conductivity $\sigma(\omega)$ (where ω is the angular frequency) has been measured for a number of Mott insulators during searches for relevant excitations in the real part of the optical conductivity $\sigma_1(\omega)$. Organic-salt Mott insulators on a dimer-triangular lattice, such as $\kappa\text{-(BEDT-TTF)}_2\text{Cu}_2(\text{CN})_3$, where BEDT-TTF stands for bis(ethylenedithio)tetrathiafulvalene,

¹Department of Physics, Yonsei University, Seoul, Republic of Korea. ²Department of Physics and Astronomy, Rutgers University, Piscataway, NJ, USA. ³Rutgers Center for Emergent Materials, Rutgers University, Piscataway, NJ, USA. ⁴Korea Atomic Energy Research Institute, Daejeon, Republic of Korea. ⁵School of Computational Sciences, Korea Institute for Advanced Study, Seoul, Republic of Korea. ⁶Department of Physics, Korea Advanced Institute of Science and Technology, Daejeon, Republic of Korea. ⁷Present address: Department of Chemistry, Princeton University, Princeton, NJ, USA. ⁸These authors contributed equally: Taek Sun Jung, Xianghan Xu, Jaewook Kim.  e-mail: egmoon@kaist.ac.kr; sangc@physics.rutgers.edu; super@yonsei.ac.kr

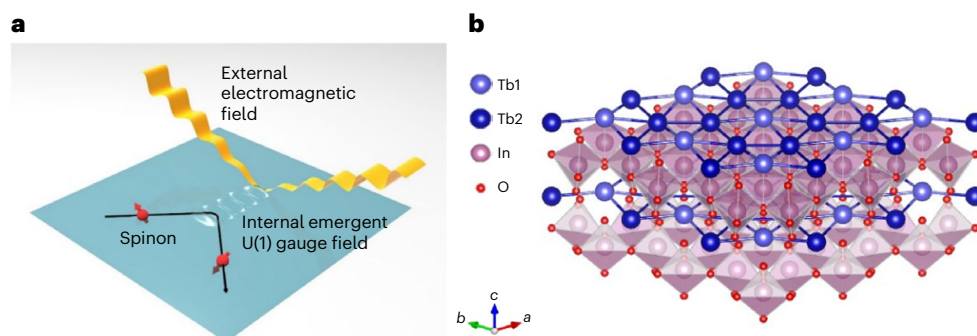


Fig. 1 TbInO_3 as a QSL candidate. **a**, Schematic picture for the mechanism of interaction between spinons and the external electromagnetic field via an internal emergent U(1) gauge field. **b**, The crystal structure of TbInO_3 . The quasi-two-dimensional triangular layer of Tb ions, which can harbour spin frustration,

is placed along the ab plane between InO_3 layers. Each Tb1 ion is placed at the centre of the hexagon whose vertices are occupied by the nearest-neighbour Tb2 ions.

were reported to have $\sigma_1(\omega) \propto \omega^a$ with $a = 0.8\text{--}1.5$ (ref. 23) whereas no notable in-gap absorption was reported for the triangular lattice YbMg-GaO_4 (ref. 24). In the kagome lattice herbertsmithite $\text{ZnCu}_3(\text{OH})_6\text{Cl}_2$, a power-law dependence was observed with a variable power exponent close to 1.4 (ref. 25). Despite the clear presence of such excitations within the Mott gap, identification of their true nature has been hampered by deviations from the quadratic frequency dependence $\sigma_1(\omega) \propto \omega^2$ predicted for certain classes of QSLs and by disorder and impurity issues²⁶. Also note that all the power-law dependences have been observed so far only at low temperatures of a few kelvins, in accordance with the common belief that QSL behaviour occurs only at extremely low temperatures.

Here, we report the unconventional dynamics of exotic emergent excitations in TbInO_3 detected with terahertz time-domain spectroscopy (THz-TDS). The power-law behaviour $\sigma_1(\omega) \propto \omega^2$ in the terahertz region was obtained over the entire temperature range of 1.5–300 K, with the power index equal to 2.0009 ± 0.0057 . Furthermore, a dramatic Fano interference pattern was clearly observed in an infrared-active phonon mode, indicating a continuous spectrum of emergent excitations strongly interacting with the phonon mode. We found that the excitation continuum is insensitive to the formation of crystal-field transitions (CFTs) below 150 K and robust against external magnetic fields up to 7 T. Our terahertz spectroscopic investigations thus establish TbInO_3 as an archetypal Mott insulator whose exotic emergent carriers are coherent even at room temperature.

TbInO_3 crystallizes into a hexagonal structure, consisting of alternating layers of TbO_6 and InO_3 polyhedra along the c axis (Fig. 1b). Tb^{3+} ions form a quasi-two-dimensional triangular lattice with two different sites: the Tb2 sites form a honeycomb structure, and the Tb1 sites are at the centre of the hexagons. An imbalance in the populations and opposite shifts along the c axis of the two Tb sites lead to ferroelectric polarization and topological vortex domains²⁷. The magnetic susceptibility shows strong in-plane anisotropy without any magnetic ordering down to 0.46 K. Further studies of muon spin rotation and specific heat in TbInO_3 did not find any sign of magnetic order or spin freezing down to ~ 0.1 K, suggesting that TbInO_3 is a QSL candidate^{28,29}. Since Tb^{3+} is a non-Kramers ion, it may have a non-magnetic ground state. Analysis of the low-energy spectra from inelastic neutron scattering from powder samples suggests that the ground states of the Tb1 and Tb2 ions are singlets and doublets, respectively, thus realizing a honeycomb spin structure²⁸. However, inelastic neutron scattering and Raman spectroscopy for single crystals suggest that both Tb sites are equivalent, thus maintaining the triangular spin structure^{29,30}.

The low-frequency optical conductivity spectra of TbInO_3 single crystals were acquired by THz-TDS (Methods). The complex transmittance coefficient was obtained with a Fourier transform from the

time-domain waveforms of the electric field component of the terahertz light polarized along the ab plane (hosting the Tb lattice) (Fig. 1b). The real $\sigma_1(\omega)$ and imaginary $\sigma_2(\omega)$ parts of the optical conductivity $\sigma(\omega)$ were extracted independently, but without using a Kramers–Kronig analysis (Methods). We used three samples with different thicknesses (500, 385 and 272 μm) to optimize the spectral range of the measurements (Methods). Figure 2a shows $\sigma_1(\omega)$, the real part of the optical conductivity, of a 500- μm -thick TbInO_3 single crystal measured at room temperature (300 K). We purposefully measured the terahertz transmissions for this thick as-grown crystal to avoid interference fringes due to multiple internal reflections within the sample. The resulting spectrum of the real part of the optical conductivity clearly exhibits a unique frequency dependence of ω^2 over a fairly broad terahertz region between 8 cm^{-1} (1 meV) and 56 cm^{-1} (7 meV). In the inset of Fig. 2a, we demonstrate the quadratic frequency dependence of $\sigma_1(\omega)$ by plotting it as a function of frequency with linear and log scales to emphasize the quadratic frequency dependence. It, indeed, shows that the power law $\sigma_1(\omega) \propto \omega^2$ is quite robust. In fact, our power-law fit of the spectrum within the central range of 13–50 cm^{-1} (1.6–6.3 meV) yielded a power index of 2.0009 ± 0.0057 within the 95% confidence margin. For this fit, we used the function $\alpha\omega^\beta + c$, where α is a parameter proportional to the excitation strength, β is a power index of frequency and c is a constant parameter representing any experimental noise. The value of c was typically $\sim 0.01 \Omega^{-1} \text{cm}^{-1}$, which is smaller than the maximum conductivity level by two orders of magnitude. Note that the power-law dependence $\sigma_1(\omega) \propto \omega^2$ actually persists to higher frequencies (Fig. 2b), although this 500- μm -thick TbInO_3 crystal suffers from a sharp reduction in transmission beyond 60 cm^{-1} due to the strong attenuation by the quadratically increasing optical conductivity spectrum.

Consequently, we took a similar TbInO_3 crystal and thinned it down to a thickness of 272 μm to broaden the transparent spectral window up to 125 cm^{-1} (16 meV) (Fig. 2b). The thinning inevitably introduced some noisy interference fringes at the low-frequency end, but the overall ω^2 behaviour can now be seen to extend to at least up to 125 cm^{-1} (16 meV). In addition, we captured the lowest infrared-active in-plane optical phonon mode, which is at 98 cm^{-1} and on top of the ω^2 background. Notably, the spectacular Fano-like distortion of the phonon lineshape observed here indicates that there was a strong interaction between the phonon mode and a continuum of excitations manifested by the ω^2 background³¹. A similar example of a strong phonon–spinon interaction has been observed in the Raman spectra of other Mott insulators, notably $\alpha\text{-RuCl}_3$ under an external magnetic field that presumably induces a QSL phase from the parent antiferromagnetic phase^{19,20,32}. Figure 2b shows the fitting of our spectrum to a combination of the power-law model and a Fano lineshape profile. The excellent fit also yields a Fano parameter of -2.66 ($1/|q| \approx 0.38$), which corresponds

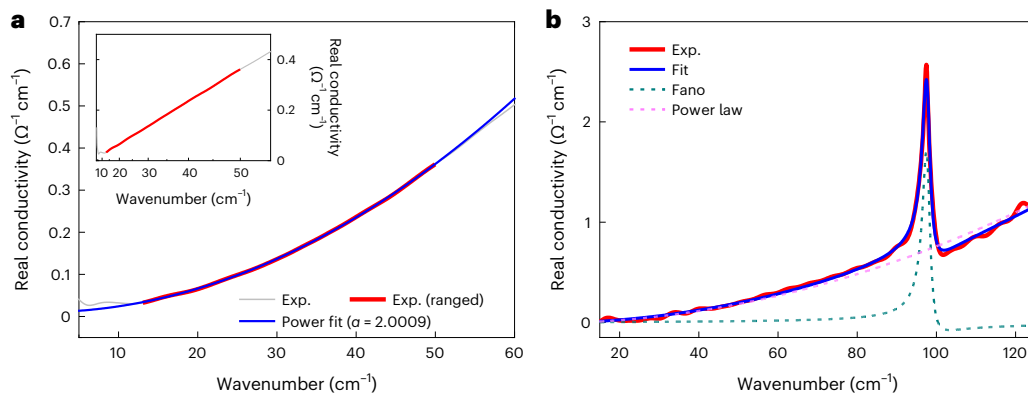


Fig. 2 | Power-law optical conductivity and Fano interference observed in TbInO₃ in the terahertz region. a, b. The real part of the optical conductivity $\sigma_1(\omega)$ has a quadratic frequency dependence for 500- μm -thick (a) and 272- μm -thick (b) crystals at room temperature. The grey lines in a represent experimental data. The red lines are part of the experimental spectrum fitted with a power law (blue line). Inset of a presents the same data versus frequency in linear and

log scales to highlight the quadratic frequency dependence. b, The red line represents experimental data whereas the blue line is a fit that incorporates a power-law component and an asymmetric Lorentzian for the Fano-distorted optical phonon mode. The fit components for the power-law conductivity and the Fano-asymmetric phonon mode are plotted separately in green and magenta, respectively. Exp., experimental.

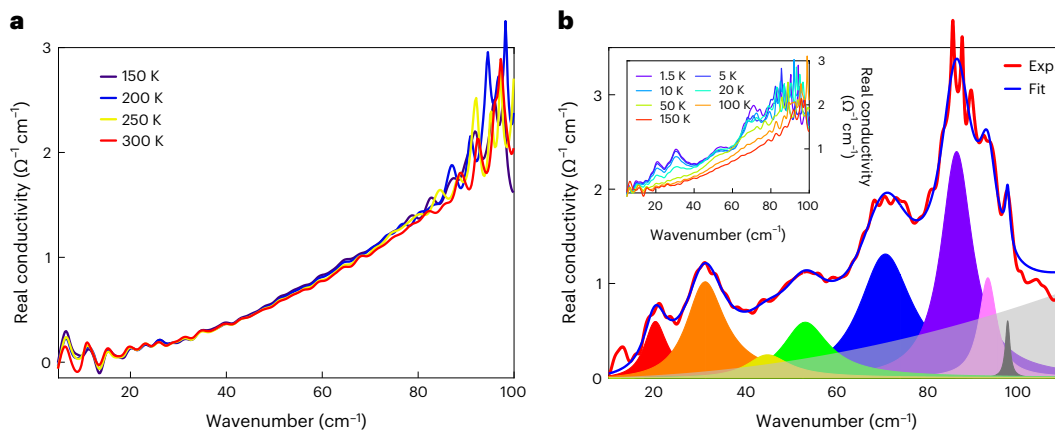


Fig. 3 | Temperature dependence of the optical conductivity of TbInO₃ in the terahertz region. a. Temperature-dependent real part of the optical conductivity $\sigma_1(\omega)$ of a 385- μm -thick TbInO₃ crystal from 300 down to 150 K. b, The inset shows $\sigma_1(\omega)$ for temperatures from 150 down to 1.5 K (the same sample as in a). The main panel shows $\sigma_1(\omega)$ of a 272- μm -thick TbInO₃ crystal

(transmitting up to 110 cm^{-1} at the high-frequency end) at 1.5 K (experimental values in red and fitted values in blue) along with decomposed fitted results for seven CFTs and one optical phonon mode. These excitations are indicated by coloured Lorentzian peaks. The shaded grey background is the power-law continuum observed at room temperature.

to stronger asymmetry than those reported in the Raman studies of other QSL candidates including $\alpha\text{-RuCl}_3$ ($1/|q| \approx 0.35$ at 1.7 K and 9 T)³² and Cu_2IrO_3 ($1/|q| \approx 0.12$ at 6 K)³³. Detailed information about the fitting model employed here is described in Methods. With the Fano interaction properly accounted for in this way, the power-law fit produces a power index of 2.0085 ± 0.0112 (within the 95% confidence margin), confirming the presence of the quadratic frequency background of the excitation continuum.

The temperature dependence of $\sigma_1(\omega)$ of a 385- μm -thick TbInO₃ crystal in the terahertz region is presented in Fig. 3a. The thickness of 385 μm was chosen to allow us to probe the temperature dependence in a fairly broad spectral range of 5–100 cm^{-1} . We did not observe practically any change in $\sigma_1(\omega)$ over the entire temperature range of 150–300 K. Below 150 K, a series of CFTs appeared in the form of absorption peaks on top of the ω^2 background. These rapidly grew in intensity as the temperature decreased (Fig. 3b, inset; the same sample as in Fig. 3a). The most intense activity of the CFTs was at 1.5 K, the lowest temperature for our measurements. The corresponding optical conductivity spectrum of a 272- μm -thick TbInO₃ crystal (transmitting up to 110 cm^{-1} at the high-frequency

end) is plotted in the main panel of Fig. 3b along with a fit to a group of eight Lorentzian peaks plus the ω^2 background of 300 K. The highest-frequency peak, at 98 cm^{-1} , is actually a replica of the optical phonon mode shown in Fig. 2b. It is at the same frequency but reduced in strength due to hybridization with the CFTs³⁰. The ground multiplet of Tb^{3+} is 7F_6 and consists of $2J + 1 = 13$ degenerate states, corresponding to $J = 6$. This multiplet splits into five singlets and four doublets by the crystal field of C_{3v} local symmetry. Therefore, eight intra-band transitions within the ground multiplet are allowed. Although the lowest transition was not detected because of the limit of our spectral range, all the other seven transitions were detected (Fig. 3b). Further, the seven peaks comprising the CFTs of the Tb ion have been thoroughly investigated in a previous Raman study³⁰, with results fully consistent with ours (Extended Data Table 1). That the overall optical conductivity spectrum can be quite well fitted with Lorentzians and a broad ω^2 background acquired at room temperature confirms that the CFTs are rather independent of the excitation continuum. This is also consistent with the assumption that the ω^2 background is independent of temperature even below 150 K all the way down to 1.5 K at least.

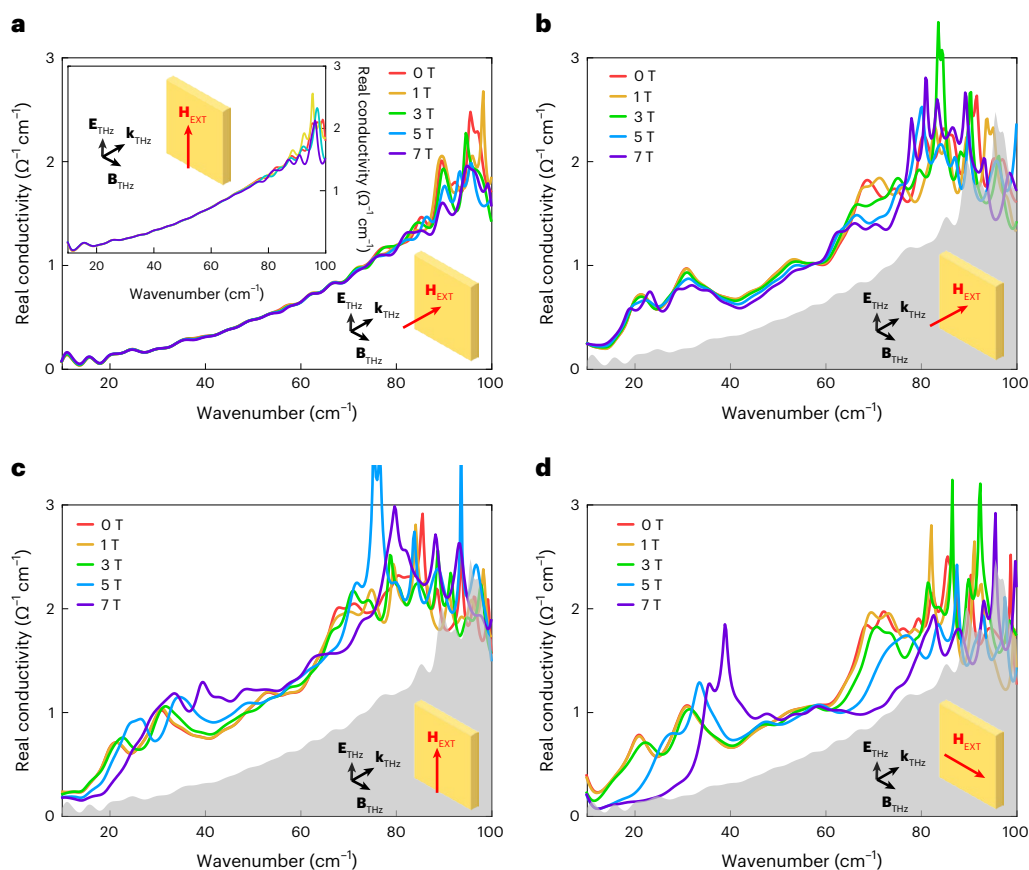


Fig. 4 | Magnetic field dependence of the optical conductivity of TbInO₃ in the terahertz region. a–d, Field-dependent real part of the optical conductivity $\sigma_1(\omega)$ of the 385- μm -thick TbInO₃ crystal for various external magnetic field configurations and temperatures. $\mathbf{k}_{\text{THz}} \parallel \mathbf{H}_{\text{EXT}} \perp \mathbf{B}_{\text{THz}}$ at 300 K (inset: $\mathbf{k}_{\text{THz}} \perp \mathbf{H}_{\text{EXT}} \perp \mathbf{B}_{\text{THz}}$) (a), $\mathbf{k}_{\text{THz}} \parallel \mathbf{H}_{\text{EXT}} \perp \mathbf{B}_{\text{THz}}$ at 1.5 K (b), $\mathbf{k}_{\text{THz}} \perp \mathbf{H}_{\text{EXT}} \perp \mathbf{B}_{\text{THz}}$ at 1.5 K (c) and $\mathbf{k}_{\text{THz}} \perp \mathbf{H}_{\text{EXT}} \parallel \mathbf{B}_{\text{THz}}$ at 1.5 K (d). The directions of the propagation wavevector \mathbf{k}_{THz} , the terahertz electric field \mathbf{E}_{THz} , the terahertz magnetic field \mathbf{B}_{THz} and the

external magnetic field \mathbf{H}_{EXT} are shown in the right lower corners. In a, the room-temperature optical conductivity is almost unchanged under an external magnetic field of up to 7 T. The room-temperature optical conductivity acquired in the absence of an external magnetic field is also plotted as a grey filled curve in b–d. CFTs observed at 1.5 K show varied dependences under an external magnetic field.

Note that the present terahertz data acquired at room temperature are to be interpreted in the framework of the triangular-lattice configuration of TbInO₃. According to a report by Clark et al.²⁸, TbInO₃ has a slightly distorted triangular lattice or, more accurately, a stuffed honeycomb lattice in which Tb1 ions are the centres of the surrounding honeycomb lattice formed by Tb2 ions. Below 7.5 K, which matches the energy splitting between the ground singlet and the first excited doublet of Tb1 ions (−0.65 meV), the thermally isolated singlet ground state of Tb1 becomes magnetically inactive, thereby resulting in an effective hexagonal lattice consisting of Tb2 ions with a doublet crystal-field ground state. We believe that this scenario for $T < 7.5$ K is essentially irrelevant to the excitation continuum already found at room temperature. On the other hand, Ye et al. reported the fully doublet ground state nature without the singlet composition of the Tb1 ions in TbInO₃ through an entropy analysis of crystal-field excitations from each possible ground state³⁰.

Finally, we found an intriguing invariability of the ω^2 behaviour under external magnetic fields of up to 7 T, as shown in Fig. 4 for the 385- μm -thick TbInO₃ crystal. We do not see any field dependence at room temperature (Fig. 4a and Extended Data Fig. 1) or at 1.5 K (Fig. 4b–d). The only magnetic field effects observed are the shifts and splittings of the CFT lines. This insensitivity to external magnetic fields removes the possibility that the ω^2 background is due to paramagnetic impurities. Note that a similar invariability under an external magnetic

field at low temperature ($T = 6$ K) was also reported by Pilon et al.²⁵ for herbertsmithite (ZnCu₂(OH)₆Cl₂), with its excitation continuum also attributed to the spinon continuum.

We stress that the quadratic frequency dependence of the real part of the optical conductivity, $\sigma_1(\omega) \propto \omega^2$, is extraordinary. A power-law dependence of the optical conductivity appears in quantum critical states of electrons with point-nodal systems, $\sigma_{\text{point-nodal}}(\omega) \propto \omega^{(d-2)/z}$, with a spatial dimension d and a dynamical critical exponent z (refs. 34–36). A Weyl semimetal in three spatial dimensions with a linear dispersion gives $\sigma_{\text{point-nodal}}(\omega) \propto \omega$ ($d = 3$ and $z = 1$), but the quadratic dependence is even unreachable for the quantum critical states, especially in two spatial dimensions^{37–40}. An alternative possibility may be proposed in association with strongly disordered media such as metallic Fermi glass⁴¹. However, TbInO₃ is highly crystalline, and the optical conductivity of a typical Fermi glass is about 10^{-3} smaller than that of TbInO₃, as reported here.

As a Mott insulator, TbInO₃ has a charge gap $\Delta_{\text{Mott}} \approx 2$ eV according to our optical measurements (Extended Data Fig. 2), and the main degrees of freedom are spins, orbitals and phonons with strong spin-orbit coupling, which is typically of the order of 0.1–0.2 eV (800–1,600 cm^{-1}) in magnitude⁴². The unique power-law dependence and the Fano interference indicate that the exotic carriers have a continuous spectrum. Acoustic phonons can be ruled out because they cannot couple to external electromagnetic waves of zero wavevector. It is

also incomprehensible that acoustic phonons could interact with the optical phonons to produce Fano interferences. Indeed, the absence of a temperature dependence in $\sigma_1(\omega)$ of TbInO_3 is inconsistent with any phonon mechanisms. Thus, we conclude that the quadratic frequency dependence originates from the spin and orbital degrees of freedom.

One intriguing proposal for the characteristic power law based on spin and orbital degrees of freedom is associated with the possibility of QSLs. Indeed, the quadratic frequency dependence was predicted for a class of QSLs²⁶, including the U(1) Dirac spin liquid and quantum critical spinons. It is natural to assign fermionic and bosonic excitations to be the exotic emergent carriers exhibiting the unique quadratic frequency dependence here. Similarly, note that the magnitude of $\sigma_1(\omega)$ per layer at $\omega/2\pi c = 1$ THz is about $10^{-4} e^2/h$ in TbInO_3 , which is like the $10^{-4} e^2/h$ of herbertsmithite ($\text{ZnCu}_3(\text{OH})_6\text{Cl}_2$)²⁵, in comparison with the theoretical estimate $10^{-5} e^2/h$ for the latter material²⁶.

Though it is tempting to accept the QSL scenarios, important issues remain to be resolved. The hierarchy of energy scales needs to be scrutinized. The observed quadratic frequency dependence survives up to room temperature, which is larger than the magnetic exchange interactions estimated from first-principles calculations⁴³. Also, the direct application of the previous theoretical predictions needs some caution. For example, a spin current is not well defined under the strong spin-orbit interaction, and thus, the previous spinon spin current mechanism for the quadratic frequency dependence may be inapplicable at face value²⁶. Similarly, spin degrees of freedom of an effective spin-only model with a Curie–Weiss temperature of -20 K cannot explain the quadratic frequency dependence of TbInO_3 at room temperature. Yet, the applicability of the effective spin-only model is not well established in TbInO_3 , and its low-temperature physics described in that context is highly questionable. After all, the Curie–Weiss temperature is obtained by analysing the high-temperature behaviour of magnetic susceptibility, which shows strong anisotropic behaviour. Such anisotropy indicates the possibility that ‘multiple’ energy scales might play a role in TbInO_3 . In fact, such multiple energy scales commonly appear near Mott transitions, as reported in the literature⁴⁴. In previous studies based on density functional theory⁴³, the large Hubbard U term (estimated to be -6 eV) was shown to be crucial. Moreover, the spin–orbit interaction is known to be strong (0.1 – 0.2 eV)⁴². Therefore, we believe that a more thorough understanding beyond the effective spin-only model is necessary to identify the precise nature of the local degree of freedom associated with the quadratic frequency dependence in TbInO_3 .

Our experimental data provide convincing evidence for exotic room-temperature carriers in TbInO_3 . Strong geometric frustration and spin–orbit coupling in TbInO_3 are expected to play a vital role, and future theoretical and experimental works incorporating strong spin–orbit coupling from the beginning are highly desirable. For example, it would be intriguing to find out how the exotic charge carriers convey energy or heat and whether the Wiedemann–Franz law is violated as a result. Furthermore, our observation of the quadratic frequency dependence in the optical conductivity and the Fano asymmetry of phonons confirms that the exotic emergent charge carriers may survive even at room temperature, which opens up new possibilities for probing and controlling highly entangled QSL states in ambient conditions.

Online content

Any methods, additional references, Nature Portfolio reporting summaries, source data, extended data, supplementary information, acknowledgements, peer review information; details of author contributions and competing interests; and statements of data and code availability are available at <https://doi.org/10.1038/s41567-023-02174-5>.

References

- Mott, N. F. The basis of the electron theory of metals, with special reference to the transition metals. *Proc. Phys. Soc. A* **62**, 416–422 (1949).
- Mott, N. F. Metal-insulator transition. *Rev. Mod. Phys.* **40**, 677–683 (1968).
- Mott, N. F. Metal-insulator transitions. *Contemp. Phys.* **14**, 401–413 (1973).
- Imada, M., Fujimori, A. & Tokura, Y. Metal-insulator transitions. *Rev. Mod. Phys.* **70**, 1039–1263 (1998).
- Amico, L., Fazio, R., Osterloh, A. & Vedral, V. Entanglement in many-body systems. *Rev. Mod. Phys.* **80**, 517–576 (2008).
- Anderson, P. W. Resonating valence bonds: a new kind of insulator? *Mater. Res. Bull.* **8**, 153–160 (1973).
- Lee, P. A. An end to the drought of quantum spin liquids. *Science* **321**, 1306–1307 (2008).
- Balents, L. Spin liquids in frustrated magnets. *Nature* **464**, 199–208 (2010).
- Zhou, Y., Kanoda, K. & Ng, T.-K. Quantum spin liquid states. *Rev. Mod. Phys.* **89**, 025003 (2017).
- Savary, L. & Balents, L. Quantum spin liquids: a review. *Rep. Prog. Phys.* **80**, 016502 (2017).
- Broholm, C. et al. Quantum spin liquids. *Science* **367**, eaay0668 (2020).
- Yamashita, M. et al. Highly mobile gapless excitations in a two-dimensional candidate quantum spin liquid. *Science* **328**, 1246–1248 (2010).
- Han, T. H. et al. Fractionalized excitations in the spin-liquid state of a kagome-lattice antiferromagnet. *Nature* **492**, 406–410 (2012).
- Kitaev, A. Anyons in an exactly solved model and beyond. *Ann. Phys.* **321**, 2–111 (2006).
- Ross, K. A., Savary, L., Gaulin, B. D. & Balents, L. Quantum excitations in quantum spin ice. *Phys. Rev. X* **1**, 021002 (2011).
- Chillal, S. et al. Evidence for a three-dimensional quantum spin liquid in $\text{PbCuTe}_2\text{O}_6$. *Nat. Commun.* **11**, 2348 (2020).
- Banerjee, A. et al. Neutron scattering in the proximate quantum spin liquid α - RuCl_3 . *Science* **356**, 1055–1059 (2017).
- Helton, J. S. et al. Spin dynamics of the spin-1/2 kagome lattice antiferromagnet $\text{ZnCu}_3(\text{OH})_6\text{Cl}_2$. *Phys. Rev. Lett.* **98**, 107204 (2007).
- Sandilands, L. J., Tian, Y., Plumb, K. W., Kim, Y.-J. & Burch, K. S. Scattering continuum and possible fractionalized excitations in α - RuCl_3 . *Phys. Rev. Lett.* **114**, 147201 (2015).
- Glamazda, A., Lemmens, P., Do, S.-H., Kwon, Y. S. & Choi, K.-Y. Relation between Kitaev magnetism and structure in α - RuCl_3 . *Phys. Rev. B* **95**, 174429 (2017).
- Li, G. et al. Raman spectroscopy evidence for dimerization and Mott collapse in α - RuCl_3 under pressures. *Phys. Rev. Mater.* **3**, 023601 (2019).
- Mai, T. T. et al. Polarization-resolved Raman spectroscopy of α - RuCl_3 and evidence of room-temperature two-dimensional magnetic scattering. *Phys. Rev. B* **100**, 134419 (2019).
- Elsässer, S., Wu, D., Dressel, M. & Schlueter, J. A. Power-law dependence of the optical conductivity observed in the quantum spin-liquid compound κ -(BEDT-TTF) $_2\text{Cu}_2(\text{CN})_3$. *Phys. Rev. B* **86**, 155150 (2012).
- Zhang, X. et al. Hierarchy of exchange interactions in the triangular-lattice spin liquid YbMgGaO_4 . *Phys. Rev. X* **8**, 031001 (2018).
- Pilon, D. V. et al. Spin-induced optical conductivity in the spin-liquid candidate herbertsmithite. *Phys. Rev. Lett.* **111**, 127401 (2013).
- Potter, A. C., Senthil, T. & Lee, P. A. Mechanisms for sub-gap optical conductivity in herbertsmithite. *Phys. Rev. B* **87**, 245106 (2013).
- Kim, J. et al. Spin liquid state and topological structural defects in hexagonal TbInO_3 . *Phys. Rev. X* **9**, 031005 (2019).

28. Clark, L. et al. Two-dimensional spin liquid behaviour in the triangular-honeycomb antiferromagnet TbInO_3 . *Nat. Phys.* **15**, 262–268 (2019).
29. Kim, M. G. et al. Spin-liquid-like state in pure and Mn-doped TbInO_3 with a nearly triangular lattice. *Phys. Rev. B* **100**, 024405 (2019).
30. Ye, M. et al. Crystal-field excitations and vibronic modes in the triangular-lattice spin-liquid candidate TbInO_3 . *Phys. Rev. B* **104**, 085102 (2021).
31. Fano, U. Effects of configuration interaction on intensities and phase shifts. *Phys. Rev.* **124**, 1866–1878 (1961).
32. Sahasrabudhe, A. et al. High-field quantum disordered state in $\alpha\text{-RuCl}_3$: spin flips, bound states, and multiparticle continuum. *Phys. Rev. B* **101**, 140410 (2020).
33. Pal, S. et al. Probing signatures of fractionalization in the candidate quantum spin liquid Cu_2IrO_3 via anomalous Raman scattering. *Phys. Rev. B* **104**, 184420 (2021).
34. Hosur, P., Parameswaran, S. A. & Vishwanath, A. Charge transport in Weyl semimetals. *Phys. Rev. Lett.* **108**, 046602 (2012).
35. Bácsı, Á. & Virosztek, A. Low-frequency optical conductivity in graphene and in other scale-invariant two-band systems. *Phys. Rev. B* **87**, 125425 (2013).
36. Pronin, A. V. & Dressel, M. Nodal semimetals: a survey on optical conductivity. *Phys. Status Solidi* **258**, 2000027 (2021).
37. Timusk, T., Carbotte, J. P., Homes, C. C., Basov, D. N. & Sharapov, S. G. Three-dimensional Dirac fermions in quasicrystals as seen via optical conductivity. *Phys. Rev. B* **87**, 235121 (2013).
38. Ashby, P. E. C. & Carbotte, J. P. Chiral anomaly and optical absorption in Weyl semimetals. *Phys. Rev. B* **89**, 245121 (2014).
39. Xu, B. et al. Optical spectroscopy of the Weyl semimetal TaAs. *Phys. Rev. B* **93**, 121110 (2016).
40. Chen, R. Y. et al. Optical spectroscopy study of the three-dimensional Dirac semimetal ZrTe_5 . *Phys. Rev. B* **92**, 075107 (2015).
41. Mahmood, F., Chaudhuri, D., Gopalakrishnan, S., Nandkishore, R. & Armitage, N. P. Observation of a marginal Fermi glass. *Nat. Phys.* **17**, 627–631 (2021).
42. Williams, A. F. *A Theoretical Approach to Inorganic Chemistry* (Springer, 1979).
43. Gordon, E. E. et al. Nonequivalent spin exchanges of the hexagonal spin lattice affecting the low-temperature magnetic properties of RInO_3 (R = Gd, Tb, Dy): importance of spin–orbit coupling for spin exchanges between rare-earth cations with nonzero orbital moments. *Inorg. Chem.* **57**, 9260–9265 (2018).
44. Senthil, T. & Lee, P. A. Coherence and pairing in a doped Mott insulator: application to the cuprates. *Phys. Rev. Lett.* **103**, 076402 (2009).

Publisher's note Springer Nature remains neutral with regard to jurisdictional claims in published maps and institutional affiliations.

Open Access This article is licensed under a Creative Commons Attribution 4.0 International License, which permits use, sharing, adaptation, distribution and reproduction in any medium or format, as long as you give appropriate credit to the original author(s) and the source, provide a link to the Creative Commons license, and indicate if changes were made. The images or other third party material in this article are included in the article's Creative Commons license, unless indicated otherwise in a credit line to the material. If material is not included in the article's Creative Commons license and your intended use is not permitted by statutory regulation or exceeds the permitted use, you will need to obtain permission directly from the copyright holder. To view a copy of this license, visit <http://creativecommons.org/licenses/by/4.0/>.

© The Author(s) 2023

Methods

Sample fabrication

TbInO₃ single crystals were grown in a laser-floating-zone furnace (LD-FZ-5-200-VPO-PC, Crystal Systems) under a pressurized O₂ atmosphere. Feed rods for the growth were prepared via a conventional solid-state reaction method in air. Powders of Tb₄O₇ and In₂O₃ were mixed, ground and sintered at 1,400 °C for 36 h with subsequent intermediate grindings. The resulting crystal boule was cleaved along the *ab* plane for the terahertz optical measurements.

THz-TDS setup

THz-TDS was conducted with a fibre-coupled terahertz system (TERA K15, Menlo Systems GmbH, Germany) coupled with a magneto-optical cryostat (SpectromagPT, Oxford Instruments, UK). The cryostat has four windows for optical access, a temperature range from 1.5 to 300 K and a magnetic field range from 0 to 7 T. All optical paths outside the cryostat were in an acrylic box filled with dry nitrogen purging gas to prevent water moisture from absorbing the terahertz light. The terahertz transmittance spectrum was obtained from the time-domain signal with a fast Fourier transform. The transmittance \tilde{t} through a TbInO₃ crystal was obtained by dividing the transmission spectrum of the sample by that of vacuum (empty sample holder):

$$\tilde{t} = \frac{4\tilde{N}}{(\tilde{N}+1)^2} \exp(2\pi i(\tilde{N}-1)\omega d/c)$$

where \tilde{N} is the complex refractive index of the sample along the *ab* plane, ω is the angular frequency, d is the sample thickness and c is the speed of light in vacuo. The secondary components of any internally reflected 'echo signals' that may have been picked up during transmission measurements were cut off from the time window used for data processing. This prevented any interference-related features from blurring our transmittance spectra. The THz-TDS technique employed here then yielded the real and imaginary parts of \tilde{t} separately without a Kramers–Kronig analysis. The complex refractive index \tilde{N} was obtained from \tilde{t} by numerical inversion. The complex conductivity $\tilde{\sigma}(\omega)$ can be obtained from \tilde{N} according to the formula:

$$\tilde{\sigma}(\omega) = \frac{\omega}{4\pi i} (\tilde{N}^2 - 1).$$

Optimization of the sample thickness and the spectral range of measurement

For transmission measurements using THz-TDS, one has to carefully optimize the thickness of the sample. In general, for an insulating sample, a thick film is desirable. When a terahertz pulse propagating inside a sample meets the sample–vacuum interface, it splits into two components: one transmitted into the vacuum and the other reflected back into the sample. The latter component comes back (with reduced intensity) after a one round trip of twice the sample thickness and splits again. Such internally reflected components also eventually transmit and reach the detector, generating interference fringes. One can remove them by limiting the measurement window in time to cut off such echo signals, but this requires a thick film such that the echo signals are sufficiently separated in time relative to the main transmission. For TbInO₃, the low-frequency end exhibits a low level of absorption, and an optimized sample thickness of 500 μm enabled us to reliably probe the low-frequency region while minimizing interference although the high-frequency region cannot be reliably probed due to its low intensity resulting from large absorbance of a thick sample (Fig. 2a).

For a conducting or highly absorbing sample, a thin film is desirable for attaining a transmitted signal of sufficient intensity over a wide frequency range. In this case, the echo signals quickly died out inside the sample, so interference was, typically, minimal. For TbInO₃, an optimized sample thickness of 272 μm enabled us to reach

125 cm⁻¹ as the high-frequency limit (Fig. 2b). In this way, we were able to capture an optical phonon near 100 cm⁻¹ that strongly interacted with the excitation continuum, which was otherwise masked by the absorbance of a thick sample. Finally, when measuring the transmission to test the temperature and magnetic effects, it was important to focus on the intermediate-frequency region to assess the overall effect of temperature and an external magnetic field. An optimized sample thickness of 385 μm enabled us to achieve this purpose (Fig. 3). Although both the low- and high-frequency ends suffer from noise in this intermediate-thickness sample, we could clearly confirm that the overall absorption did not change with temperature down to 150 K or with external magnetic field up to 7 T.

Fano analysis

In the main text, we used a Fano–Lorentzian model to fit the asymmetric optical phonon mode. The Fano interaction is observed when resonant scattering interferes with a background continuum state³². In our case, the spinon continuum is the background state. The low-frequency side of the spectral weight of the lowest optical phonon mode was reinforced, whereas the high-frequency side was reduced. This particular asymmetric behaviour is known to occur when the Fano-asymmetry parameter is negative⁴⁵. Previous reports of the spinon-origin Fano behaviour of optical phonon modes in other QSL candidate materials also show the same type of asymmetry^{32,33}. To fit the actual lineshape, we employed the formula introduced in ref. 46:

$$\sigma_1(\omega) = \frac{A}{60\gamma} \frac{q^2 + 2q(\omega - \omega_0)/\gamma - 1}{q^2 [1 + 4(\omega - \omega_0)^2/\gamma^2]}$$

where A is the strength parameter, γ is the scattering rate, q is the asymmetry parameter and ω_0 is the resonance frequency.

Data availability

Source data are provided with this paper. The data that support the findings of this study are available from the corresponding authors upon reasonable request.

References

- Ott, C. et al. Lorentz meets Fano in spectral line laser control. *Science* **340**, 716–720 (2013).
- Schafgans, A. A. et al. Phonon splitting and anomalous enhancement of infrared-active modes in BaFe₂As₂. *Phys. Rev. B* **84**, 052501 (2011).

Acknowledgements

The work at Yonsei University was supported by the National Research Foundation of Korea (grant no. 2017R1A5A1014862), the SRC (Science Research Center) programme of the van der Waals Materials Research Center (grant no. 2022R1A2C1006740) and the Samsung Science and Technology Foundation (grant no. SSTF-BA2102-04). The work at Rutgers University was supported by the Center for Quantum Materials Synthesis and funded by the Gordon and Betty Moore Foundation's EPIQS initiative (grant no. GBMF10104) and by the US Department of Energy (grant no. DE-FG02-07ER46382). The work at the Korea Institute for Advanced Study was supported by an individual grant (no. CG068702). T.S.J. was supported by BK-21 FOUR (Fostering Outstanding Universities for Research) and funded by the National Research Foundation of Korea under the Ministry of Education of Korea. J.K. was supported by the internal R&D programme of the Korea Atomic Energy Research Institute (grant no. 524460-23). E.-G.M. was supported by the National Research Foundation of Korea and funded by the Ministry of Science and ICT (grant nos. 2021R1A2C4001847 and 2022M3H4A1A04074153) and the National Measurement Standard Services and Technical Services for SME funded by the Korea Research Institute of Standards and Science (grant no. GP2022-0014).

Author contributions

T.S.J. performed the optical measurements. X.X. and J.K. grew the single crystal of TbInO_3 and characterized its physical properties. B.H.K. provided the theoretical analysis of CFTs. H.J.S. and Y.J.C. grew the polycrystalline TbInO_3 . T.S.J., E.-G.M. and J.H.K. analysed the data and wrote the original draft. All authors participated in the discussions and edited the manuscript. E.-G.M., S.-W.C. and J.H.K. supervised this project.

Competing interests

The authors declare no competing interests.

Additional information

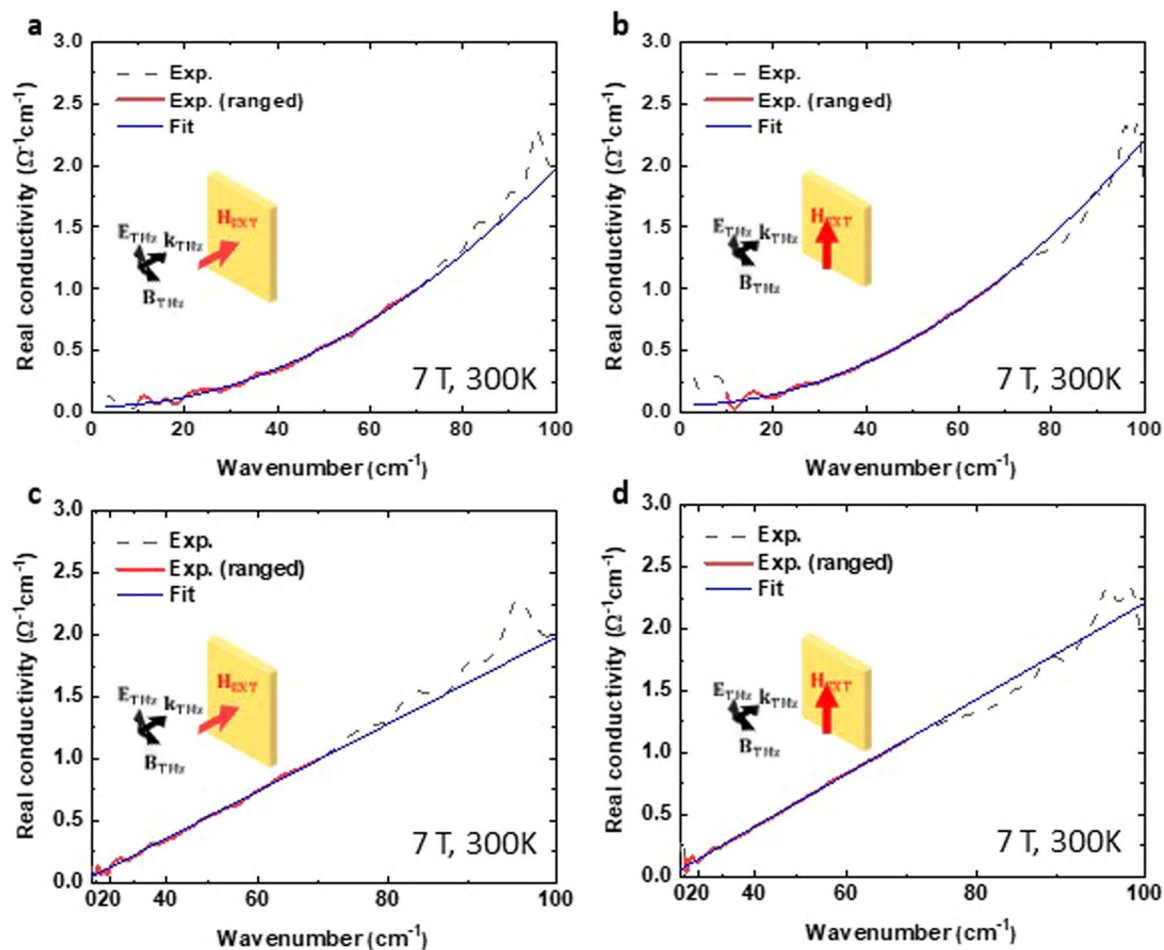
Extended data Extended data is available for this paper at <https://doi.org/10.1038/s41567-023-02174-5>.

Supplementary information The online version contains supplementary material available at <https://doi.org/10.1038/s41567-023-02174-5>.

Correspondence and requests for materials should be addressed to Eun-Gook Moon, Sang-Wook Cheong or Jae Hoon Kim.

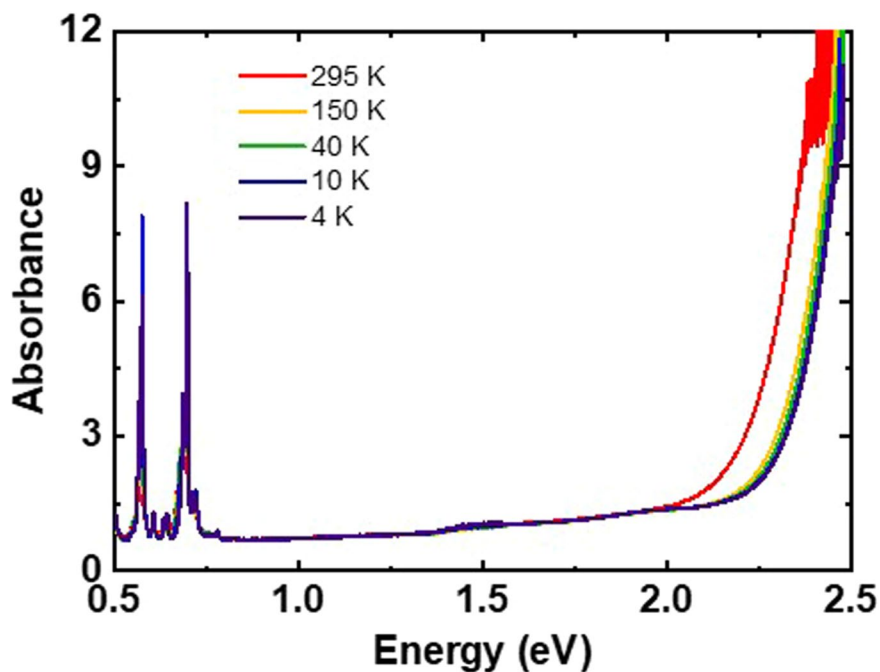
Peer review information *Nature Physics* thanks Liuyan Zhao and the other, anonymous, reviewer(s) for their contribution to the peer review of this work.

Reprints and permissions information is available at www.nature.com/reprints.



Extended Data Fig. 1 | Quadratic fit results of the real conductivity of TbInO_3 under an external magnetic field of 7 T at 300 K. Experimental real conductivity of TbInO_3 and the quadratic fit results under an external magnetic field of 7 T at 300 K for $k_{\text{THz}} \parallel H_{\text{EXT}} \perp B_{\text{THz}}$ (a) and $k_{\text{THz}} \perp H_{\text{EXT}} \perp B_{\text{THz}}$ (b). c,d, Replotted

a and b, respectively, vs. frequency in linear-log scale to highlight the quadratic frequency dependence. The dotted grey lines are the experimental spectra, the red solid lines are the fit ranges, and the blue lines are the fit results.



Extended Data Fig. 2 | Temperature dependence of the absorbance of TbInO_3 in the near-infrared and visible region. The absorbance of a 500 μm -thick TbInO_3 crystal for temperatures from 295 K down to 4 K. This experiment was conducted in an optical cryostat (Cryostat, Montana Instruments, USA) by using a grating spectrometer (Cary 5000, Agilent, USA). The low energy excitations under 1 eV are transitions to spin-orbit split multiplets, 7F_2 and

7F_0 in that order, and this result is well matched with the previous report of Raman spectroscopy³⁰. In the high energy side, a strong absorption edge was detected above 2 eV in the entire temperature range. We proposed that the large absorption edge is the Mott charge gap of TbInO_3 . This optical gap exhibits blueshift by cooling from 2.257 eV to 2.362 eV.

Extended Data Table 1 | Crystal field transitions (CFTs) and the lowest optical phonon mode

State	Ground	C1	C2	C3	C4	C5	C6	C7	C8	P1
Raman	0	6.45	20.16	29.84	45.97	50.81	70.17	87.10	92.75	X
THz	0	X	20.23	31.11	45.48	53.14	70.62	86.41	93.31	97.60

Here, we compare the energies of the CFTs and the lowest optical phonon mode as obtained from a previous Raman study³⁰ with those from our terahertz study. Our data are based on the optical conductivity spectrum of a 272 μm -thick TbInO_3 crystal measured at 1.5 K (Fig. 3b). Altogether, eight Lorentzian peaks were included for the seven CFTs (C2-C8) and the lowest optical phonon (P1). C1, the lowest CFT was not detected in our terahertz spectrum due to the lower frequency limit of our terahertz spectroscopic capacity.